J. Fluid Mech. (2003), *vol.* 477, *pp.* 339–362.
DOI: 10.1017/S0022112002003397 Printed in the United Kingdom

The Kelvin–Helmholtz to Holmboe instability transition in stratified exchange flows

By A. McC. HOGG† AND G. N. IVEY

Centre for Water Research, University of Western Australia, 35 Stirling Highway, Crawley, Western Australia 6009, Australia

(Received 21 August 2001 and in revised form 16 October 2002)

A laboratory investigation of exchange flows near the two-layer hydraulic limit is used to examine the generation of shear instability at the interface dividing the two layers. The present experiments differ from many previous investigations into shear instability, in that the instabilities are an active part of a quasi-steady flow regime rather than the product of a controlled initial state. Regimes characterized by either Kelvin–Helmholtz or Holmboe's instability are found to be separated by a well-defined transition. Observations of the transition from Kelvin–Helmholtz to Holmboe's instability are compared to predictions from scaling arguments that draw on elements of both two-layer hydraulic theory and linear stability theory. The characteristics of unstable modes near the transition, and the structure of both classes of instability are examined in detail.

1. Introduction

The role played by shear instability in the transition from laminar flow to turbulence is crucial to characterizing the evolution of density-stratified flows. Shear instability can be described as the formation of structures which draw kinetic energy out from the flow. These structures lose energy by irreversible mixing of a stable density gradient, and by turbulent dissipation. The conditions required for shear instability in a stratified fluid can be described to first order by defining a Richardson number to be the ratio of destabilizing parameters (velocity shear) to stabilizing effects (density stratification). When the Richardson number drops below a certain critical value then the flow may become unstable (Miles 1961; Howard 1961).

The most commonly studied class of instability in stratified flows is the Kelvin–Helmholtz (KH) instability (see Thorpe 1973; Koop & Browand 1979; Klaassen & Peltier 1985, for example). KH instability produces a billow which grows and rotates until secondary and convective instabilities complete the transition to turbulence. Another type of shear instability was predicted theoretically by Holmboe (1962), but has rarely been observed in experiments, and has been called Holmboe's instability (Browans & Wand 1972). This instability is composed of a pair of oppositely propagating modes which interact to produce limited mixing of the background density gradient.

In this paper we present results of laboratory experiments which enable us to examine the transition from KH to Holmboe's instability. These instabilities are

† Present address: Southampton Oceanography Centre, European Way, Southampton SO14 3ZH, UK.

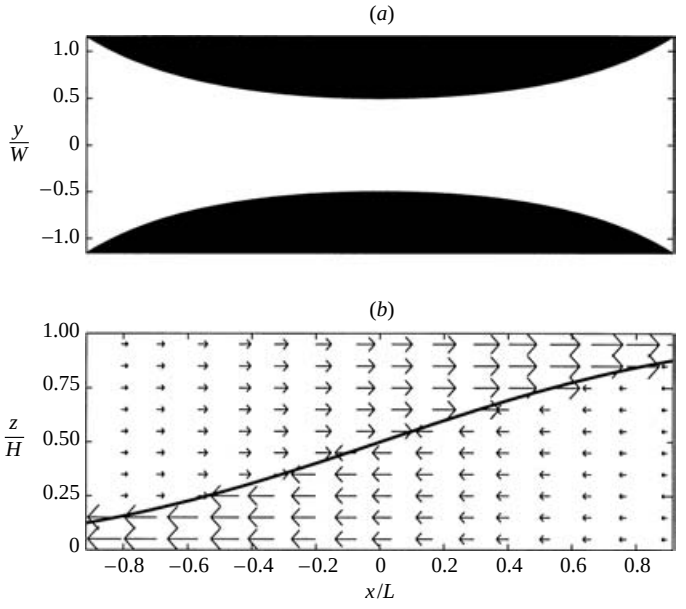

FIGURE 1. Hydraulic solution for exchange flow through a contracting channel. (*a*) Channel in plan view; (*b*) velocity vectors and interface position in elevation view.

observed in a bi-directional exchange flow which resembles the two-layer hydraulic solution (Armi 1986) for exchange flow through a contraction. Before describing the experiments we give a basic description of hydraulic exchange flows, as well as providing a brief overview of shear flow instability, and the KH–Holmboe transition.

1.1. *Two-layer hydraulic exchange flows*

The steady-state solution for density-driven exchange flow through a contracting channel is originally due to Wood (1970), with further major developments from Armi (1986), Lawrence (1990) and Dalziel (1991). This solution is derived simply from the conservation of energy and mass in a two-layer, inviscid, non-diffusive fluid, and is frequently referred to as the two-layer hydraulic solution. This hydraulic solution cannot be applied to the initiation or time dependence of exchange flow; however experiments have shown that it is a good approximation for steady flows (Wood 1970; Armi 1986; Lawrence 1993; Helfrich 1995; Zhu & Lawrence 2000). The hydraulic solution for the case of a flat-bottomed channel with a simple contraction, derived by following Lawrence (1990) is shown in figure 1. Interested readers can refer to the above references for a detailed understanding of the physics of this flow. It is sufficient for the purposes of this paper to note that, if the volume flux in each direction is equal, the difference in velocity between the two layers is constant in the streamwise (x) direction, and is given by

$$\Delta U = u_1 - u_2 = (g'H)^{1/2}, \tag{1.1}$$

where $u_i(x)$ is the layer velocity which is constant in z, H is fluid height and $g' = g\Delta\rho/\rho_0$ is the reduced gravity based on the density difference $\Delta\rho$ between the layers, the gravitational acceleration g and reference density ρ_0. Furthermore,

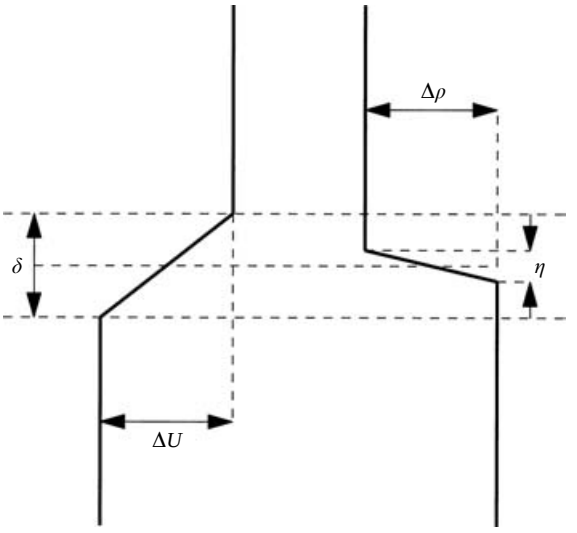

FIGURE 2. Piecewise profiles of velocity and density used for stability calculations.

the arithmetic mean velocity at any point, given by

$$\bar{U}(x) = \frac{u_1 + u_2}{2}, \tag{1.2}$$

is always directed away from the centre of the contracting region.

The derivation of the hydraulic solution requires that there is no communication between the two layers via either viscous effects or diffusion. This assumption is clearly unrealistic, and Lawrence (1990) demonstrates that the solution shown in figure 1 is only marginally stable to long waves along the entire channel. Turbulent mixing has been observed in laboratory experiments (Wood 1970) and field investigations (Gregg & Özsoy 2002). Numerical simulations (Winters & Seim 2000; Hogg, Ivey & Winters 2001*a*) show that mixing and communication between the layers is crucial to predicting the flux, which decreases as the intensity of vertical mixing increases. However, for small rates of mixing the hydraulic solution is still a good approximation to the flow (Hogg *et al.* 2001*a*).

1.2. *Shear instability*

We begin our discussion of shear instability by considering a background flow with simple idealized profiles of fluid velocity and density while neglecting viscosity and diffusion. One can estimate the growth rate of linear disturbances in such a flow. The fastest growing linear wave will amplify by extracting kinetic energy from the velocity field and grow into a nonlinear instability. Therefore, the dominant wavelength and phase speed of instabilities can be predicted with some confidence simply by finding the fastest growing mode (see Lawrence, Browand & Redekopp 1991).

The background flow used here is the piecewise velocity and density profiles seen in figure 2. Based on Hazel (1972), we define the bulk Richardson number to be

$$J \equiv \frac{g'\delta}{(\Delta U)^2}, \tag{1.3}$$

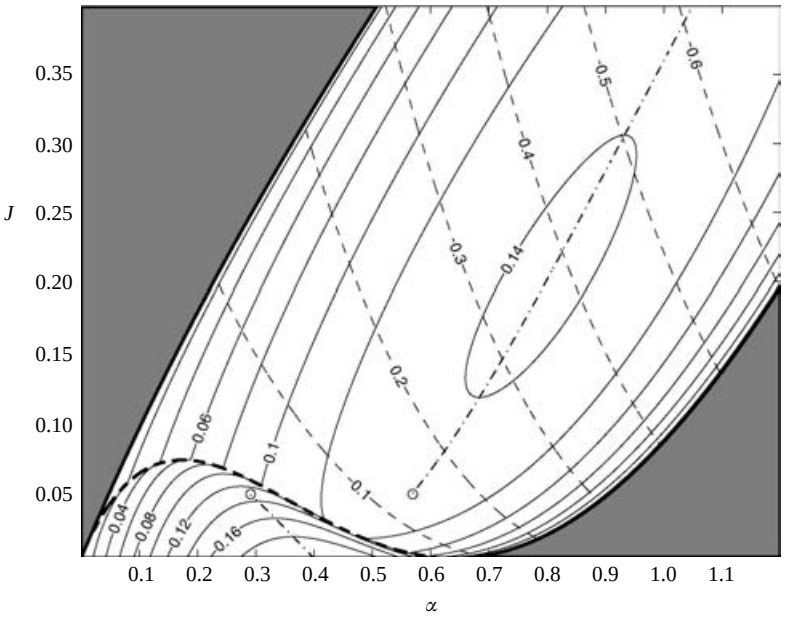

FIGURE 3. Linear stability of the configuration shown in figure 2 calculated from equations (A4)–(A7) in Haigh & Lawrence (1999), assuming $R \to \infty$. The linear stability analysis assumes perturbations of the form $\exp[i\alpha(x - ct)]$ where wavenumber α is non-dimensionalized by multiplication with the velocity interface half-thickness $\delta/2$, and phase speed c is normalized by $\Delta U/2$. Solid contours depict the non-dimensional growth rate of unstable modes ($\alpha \mathrm{Im}(c)$) as a function of J and α. The shaded regions are neutral or stable. Dashed contours show the frequency of oscillation, $\alpha \mathrm{Re}(c)$ with the heavy dashed contour indicating that phase speeds are zero below it. The dash-dot line shows the maximum growth rate as a function of J, with the transition point for KH–Holmboe modes shown as open circles.

where δ is the thickness of the shear layer. We also define the thickness of the density interface η as shown in figure 2, and the ratio of layer thicknesses $R \equiv \delta/\eta$. In the absence of viscosity and diffusion the linear stability characteristics of the flow are dependent only upon the Richardson number and R. The linear stability diagram for the case when $R \to \infty$ ($\eta = 0$) is shown in figure 3 (reproduced from Haigh & Lawrence 1999).

The key feature of figure 3 is that there are two distinct regions of instability which are divided by the heavy dashed contour in the lower left hand corner. If the most unstable mode is found beneath this dashed contour, an instability will form which has zero phase speed and relatively high growth rate. This is a KH instability (Haigh & Lawrence 1999). It occurs when the destabilizing effect of shear overcomes buoyancy, and can therefore form even when $\eta \approx \delta$ as demonstrated by Scotti & Corcos (1972) and Thorpe (1973). A KH billow is roughly symmetrical and grows to large amplitude which is limited by the formation of secondary and convective instabilities (Thorpe 1973; Smyth & Peltier 1991). The formation and dynamics of KH billows is detailed in the numerical experiments of Klaassen & Peltier (1985).

At higher values of the bulk Richardson number, the fastest growing instability is Holmboe's instability, which differs from the KH instability in several ways. First, it has a finite phase speed relative to the mean shear (Hazel 1972; Smyth, Klaassen & Peltier 1988). Secondly, growth rates are generally smaller and the rate of mixing due

to the instability is less than for KH instability (Koop & Browand 1979). Thirdly, in the absence of viscosity there is no theoretical upper limit to the Richardson number at which Holmboe's instability can occur (Holmboe 1962). It can be demonstrated (Smyth *et al.* 1988) that the instability is made up of two modes, with equal but opposite phase speed. When $R < 2.4$, the Holmboe mode is suppressed (Smyth & Peltier 1989).

Baines & Mitsudera (1994) argue that all shear instability can be derived from the phase locking of two freely propagating modes with opposite celerity. This phase locking is due to the shear, while amplification is caused by the two modes combining to kinematically increase the size of the total perturbation. For arbitrary shear profiles with a stable density gradient, while this technique recovers the same stability criteria generated by linear stability analysis, it has the advantage that it lends itself to a physical interpretation of the mechanism by which shear instability occurs. In the background flow shown in figure 2, there are four distinct freely propagating modes which can form. Two of these modes travel on the density interface (one in each direction). The other two travel on the vorticity interface, with the mode travelling on the upper interface going to the left, and the mode on the lower interface travelling right. It can be shown (Caulfield 1994; Baines & Mitsudera 1994) that when the two vorticity modes are able to lock phase, KH instability forms. However, when J is increased, the two vorticity modes are unable to communicate, because either g' is large or the distance δ between the two vorticity interfaces is large. In such cases, two unstable waves are formed by the interaction of one density mode with either one of the two vorticity modes. These two unstable modes are Holmboe's instability.

According to figure 3, when $J < 0.071$ both KH and Holmboe's instability are possible, with smaller values of Richardson number favouring KH instability and high Richardson number favouring Holmboe's instability. For $J < 0.046$, KH modes have higher growth rates, while for $0.046 < J < 0.071$, Holmboe modes grow faster (Haigh & Lawrence 1999). One therefore expects a transition between the two types of instability at $J \approx 0.046$. At the transition point, the wavelength changes discontinuously, as does the phase speed which is zero for the KH instability. This discontinuity is shown in figure 3 by the open circles on the ends of the dash-dot lines.

The above example relies on piecewise profiles which are necessarily unrealistic in order to produce an analytical solution. Smyth *et al.* (1988) use a numerical technique to find an equivalent stability diagram for cases with continuous profiles of density and velocity, finite viscosity and finite R. The stability diagram possesses similar features to figure 3, but the value of J at the KH–Holmboe transition point varies. We have performed similar calculations by defining non-dimensional profiles in velocity and density:

$$u(z) = \tanh(z), \tag{1.4}$$

$$\rho(z) = -\tanh\left(\frac{z}{R}\right), \tag{1.5}$$

and a Reynolds number of

$$Re \equiv \frac{\Delta U \delta}{4\nu}. \tag{1.6}$$

The linear stability of a viscous stratified shear flow is governed by a sixth-order eigenvalue equation originally due to Koppel (1964). Here we use Koppel's equation

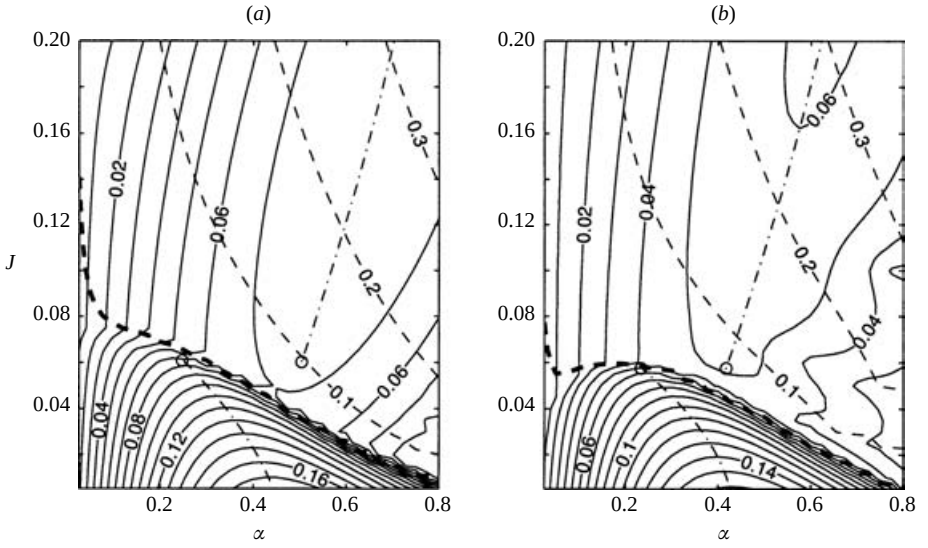

FIGURE 4. Linear stability of the configuration described by (1.4) and (1.5), found by the numerical solution of (1.7). (*a*) $R = 5$, $Re \to \infty$; (*b*) $R = 5$, $Re = 100$. Line styles are the same as for figure 3.

in the limit of large Prandtl number to write a fourth-order equation,

$$-c^2\left(\partial_z^2 - \alpha^2\right)\psi + c\left(\frac{\mathrm{i}}{\alpha Re}\left(\partial_z^2 - \alpha^2\right)^2 + 2u\left(\partial_z^2 - \alpha^2\right) - u_{zz}\right)\psi + \left(\frac{-\mathrm{i}u}{\alpha Re}\left(\partial_z^2 - \alpha^2\right)^2 - u^2\left(\partial_z^2 - \alpha^2\right) + uu_{zz} + J\rho_z\right)\psi = 0, \quad (1.7)$$

where $\psi(z)$ is the perturbation streamfunction and ∂_z represents the z-derivative. We solve this equation numerically using an identical method to that described in Winters & Riley (1992) and Hogg, Winters & Ivey (2001*b*), with rigid boundaries at the top and bottom of the fluid column. The total depth of the fluid is $H = 10\delta$.

Figure 4 shows two examples of results from this analysis. Panel (*a*) shows the inviscid case with $R = 5$, the results of which are consistent with the calculations performed by Smyth *et al.* (1988): the growth rate of Holmboe modes is reduced, and the KH–Holmboe transition occurs at higher bulk Richardson number. The introduction of viscosity makes it more difficult to numerically solve (1.7); nonetheless figure 4(*b*) shows the same general characteristics of instability. Using $Re = 100$ we find that the general trend is to damp growth rates, in particular reducing the growth rates of the higher wavenumbers. This acts to reduce the value of the wavenumber of the most unstable Holmboe mode, but does not significantly alter the position of the KH–Holmboe transition.

Several studies have investigated factors not considered by linear stability theory. The KH–Holmboe transition was investigated numerically by Smyth & Peltier (1991) with the inclusion of nonlinear effects, demonstrating that once the instability grows to a finite size, nonlinear effects play a role in determining its evolution. The two oppositely propagating Holmboe modes interact as they approach each other and mixing is accelerated by a wisp of fluid which is ejected through the cusp of the Holmboe modes. Recent numerical data (Smyth & Winters 2002) indicates that while

the growth rate of Holmboe's instability is small, the total amount of mixing due to a single instability is comparable to KH instability. This surprising result is a product of high mixing efficiency in the long-lived pre-turbulent growth phase.

The numerical experiments of Smyth & Peltier (1991) demonstrated the existence of a transition between the KH and Holmboe regimes; however characteristics of KH instability are observed on the Holmboe side of the transition in the form of complete overturning of the density interface. Likewise, on the KH side of the transition, the two counter-propagating modes are visible in the early part of the experiment, but these two modes lock phase and roll up. It is possible (Collins & Maslowe 1988; Smyth & Peltier 1991) that nonlinearity acts to increase the likelihood of interactions between modes. Such interactions effectively reduce the stability of the flow, thereby increasing the values of the bulk Richardson number at the transition point. If this type of interaction were to occur, then one would expect that the component modes of Holmboe's instability would attenuate each other as they pass, and this attenuation would increase near the KH–Holmboe transition. This consequence is tested in the present experiments.

Haigh & Lawrence (1999) also consider the effect of a vertical shift in the position of the density interface and the presence of boundaries upon the stability of the flow. It is expected that boundaries have an effect when the total fluid height $H < 10\delta$, and that the vertical asymmetry produces a difference in growth rate and phase speed between the left-going and right-going Holmboe modes (Haigh & Lawrence 1999). Nonetheless, even though these modes have different growth rates, symmetric Holmboe instabilities may still be possible, because the amplitude of the component Holmboe modes is limited by nonlinear damping, and not growth rate (Smyth *et al.* 1988).

In order to verify the predictions of linear stability theory, a number of mixing layer experiments have been conducted. For example, Scotti & Corcos (1972) demonstrated that the onset of instability could be estimated based on the Richardson number. Lawrence *et al.* (1991) used mixing layer experiments to predict the formation of asymmetric KH and Holmboe instabilities, and showed a strong correlation between observed and predicted wavelengths. Observations of the transition from KH to Holmboe modes are reported by both Koop & Browand (1979) and Lawrence *et al.* (1991); however asymmetry of the velocity and density interface positions may have affected the stability characteristics of these experiments.

The current experiments are designed to test three main issues relating to KH and Holmboe instability which remain unclear from previous studies:

(*a*) the density and velocity structure of the instabilities, in particular Holmboe's instability, as presented in § 3.1 and § 3.2;

(*b*) the extent to which J can be used to predict the type of instability which will form, and the wavelength and wave speed of that instability (results shown in § 4 and discussed in § 5);

(*c*) the extent of non-linear interactions between component modes of Holmboe's instability (results in § 3.3 with further discussion in § 5).

2. Experiments

The experiments were conducted in a $2.58 \times 0.53 \times 0.60$ m tank, with a 0.50 m long Perspex insert forming the contracting region as shown schematically in figure 5. The insert included a false bottom 0.15 m above the floor of the tank, and the contracting channel width varied smoothly from 0.12 m (at the centre) to 0.3 m. The insert was

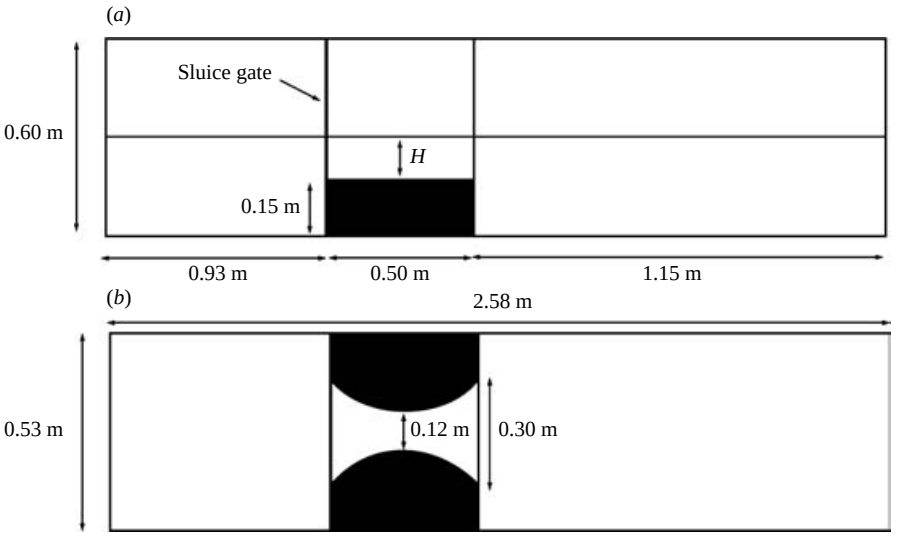

FIGURE 5. Experimental configuration. (*a*) Tank in elevation view; (*b*) plan view.

placed to the left of centre of the tank so that the reservoir on the left-hand side of the insert was 0.93 m long, and on the right-hand side was 1.15 m.

A sluice gate at the left-hand end of the insert separated fresh water in the left-hand reservoir from saline water in the right-hand reservoir. Once the sluice gate was opened, dense water flowed through the contracting channel, spilling into the left-hand reservoir and settling beneath the level of the false bottom in the test section, and as such, did not affect flow in the channel. Likewise, fresh water flowed rightwards and resided in the upper part of the right-hand reservoir. The fresh water level in the right-hand reservoir limited the duration of a given experiment. When this level became too large, it flooded the hydraulic control and altered the quasi-steady exchange flow in the contraction. The false bottom in the insert, in combination with the asymmetrical positioning of the insert, was designed to maximize the length of experiments.

The tank was filled to a level H above the floor of the channel. The sluice gate was closed and salt added to the right-hand reservoir to increase the density on that side. Experiments were initiated by lifting the sluice gate, allowing exchange between the two basins. After 20–50 s (depending on the hydraulic velocity scale given by (1.1)), the exchange reached a quasi-steady state (maximal exchange as defined by Armi & Farmer 1987). The exchange was roughly constant for between 3 and 9 min. Superimposed on this quasi-steady state, instabilities formed on the interface dividing the two layers.

Measurements of the density and velocity fields were taken during the experiments. Several attempts were made to measure the density field. First, conductivity probes were used; however these measurements were unsuccessful as these probes could not resolve the density interface. Secondly, the evolution of the interface was observed by seeding fluid in the left-hand reservoir with sodium fluorescein, a fluorescent dye. The flow was illuminated from below with a rack of 50 W halogen bulbs with a double slit arrangement producing a vertical light sheet of width between 5 and 15 mm. Images were taken with a CCD video camera placed 1.6 m from the tank perpendicular to the flow. The video images were written directly to disk using an ITEX PC-COMP

Experiment name	H (mm)	g' (m s^{-2})
S1	90	0.0189
S2	70	0.0152
S3	50	0.0187
S4	50	0.0355
A1	80	0.0221
A2	70	0.0191
A3	60	0.0193
A4	50	0.0199
K1	90	0.0179
K2	70	0.0185
K3	50	0.0186
K4	50	0.0353
P1	90	0.0195
P2	80	0.0135
P3	70	0.0157
P4	60	0.0106
P5	50	0.0209
P6	50	0.0202
P7	50	0.0353
P8	40	0.0137

TABLE 1. Experiments undertaken. Experiments S are those for taking still photographs, A refers to experiments using analogue video, K to experiments in which potassium permanganate crystals were used to estimate velocity profiles and P to PIV velocity experiments.

frame-grabber and were simultaneously stored on S-VHS tape. This technique was useful for visualizing the instabilities; however the resolution was too low to accurately measure the density interface thickness. Therefore a third technique was employed. Still photographs were taken with a Nikon F90 SLR camera with a 500 mm zoom lens, a 42 mm extension tube and using 3200 ASA black and white film. Negatives were scanned to a resolution of 1200 horizontal lines (limited by the resolution of the film), allowing an interface thickness in the fluorescein profile, η_F, to be measured by fitting a tanh function to the vertical profiles of intensity I using the definition

$$\eta_F = \frac{\Delta I}{(\partial I/\partial z)_{max}}, \tag{2.1}$$

where ΔI is the difference in intensity between the upper and lower layers. The density interface thickness η is calculated from η_F as shown in § 4.2. The external parameters for experiments which used this technique are shown in table 1, labelled by the prefix S. In this table, experiments with the prefix A are experiments used for visualizing the evolution of instabilities recorded from analogue video.

The velocity interface thickness was measured by dropping crystals of potassium permanganate of diameter 0.5–1 mm into the fluid. This technique allowed higher resolution measurements of the velocity interface than the PIV measurements outlined below. For these experiments (labelled by K in table 1) the test section was back-lit, and images were taken using colour video recorded onto S-VHS tape, and converted to a digital image using the PC-COMP frame-grabber at a later date. The crystal left a streak of dye in the fluid, allowing measurement of the fluid displacement as a function of z. By tracking the fall of the crystal it was possible to convert the displacement into a horizontal velocity profile by scaling the x-coordinates of the video image.

The interface thickness was measured directly from the velocity profile using

$$\delta = \frac{\Delta U}{(\partial U/\partial z)_{max}}. \tag{2.2}$$

To measure two-dimensional velocity fields, particle image velocimetry (PIV) was used (see Stevens & Coates 1994, for a description of the algorithm). The flow was seeded with pliolite particles of diameter 45–75 μm, and illuminated by the light sheet. Images were taken from a distance of 2.0 m using a Hamamatsu C4742 digital camera with 1017 × 996 pixels resolution and 10-bit pixel depth. The images were downloaded to a PC using an ITEX IC-DIG-16-D frame-grabber. Two images were taken at a separation of 140–150 ms which was limited by the speed of the digital camera. The first image was stored in PC RAM, and written to hard disk after both images were collected. Image pairs were taken at a separation of 1 s.

The processing of the PIV images was complicated by the high velocities in the channel relative to the frame rate of the camera. Refinements to the technique were required to determine velocity fields, although quality degenerated as fluid velocity increased. The refinements involved three phases. First, using a relatively large box size (40 pixels, or 4.8 mm), estimates of the velocity were obtained. Poor quality vectors were eliminated by applying an adaptive Gaussian filter (identical to that used by Cowen & Monismith 1997). The remaining vectors were averaged in time, and used as input velocities for a second pass of the PIV routine, allowing a reduction in the size of the search radius, and hence decreasing errors. The results of the second pass were averaged over a 20 s time interval, and these averages were used as input velocities for a third pass of PIV. The third pass allowed use of a smaller box size (16–20 pixels or 1.9–2.4 mm), and a further reduction in the search radius, resulting in higher quality measurements of regions with high velocity shear. Eight experiments were conducted using these techniques and are identified by the prefix P in table 1. Although we were unable to look at both velocity and density fields simultaneously (as was done with simultaneous PIV and laser induced fluoresence in Pawak & Armi 1998 and Zhu & Lawrence 2001), these techniques allowed visualization of the velocity and density evolution of the flow at very high spatial resolution.

3. Results

The mean flow evolution in the channel is similar to that described by Zhu & Lawrence (2001). When the sluice gate is removed, some mixing occurs at the boundary between the two fluids. Therefore, when the quasi-steady exchange flow forms, the interface contains some mixed fluid. The diffuse interface subsequently undergoes sharpening as a result of advection of interfacial fluid out of the channel, and the divergence of the fluid as it accelerates through the contraction. In some experiments a sharp stable interface forms, which is ultimately disturbed by instabilities. In such cases the timing of the onset of instability appears to be dependent upon background noise, and instability can be initiated by creating a small disturbance to the interface. In other cases the onset of instability occurs shortly after the exchange begins.

3.1. *Observations of instabilities*

Both KH and Holmboe's instability are observed in experiments S1–S4. In figure 6 we show a representative image from each of the four experiments. Estimates of bulk Richardson number and Reynolds number for each experiment are shown in

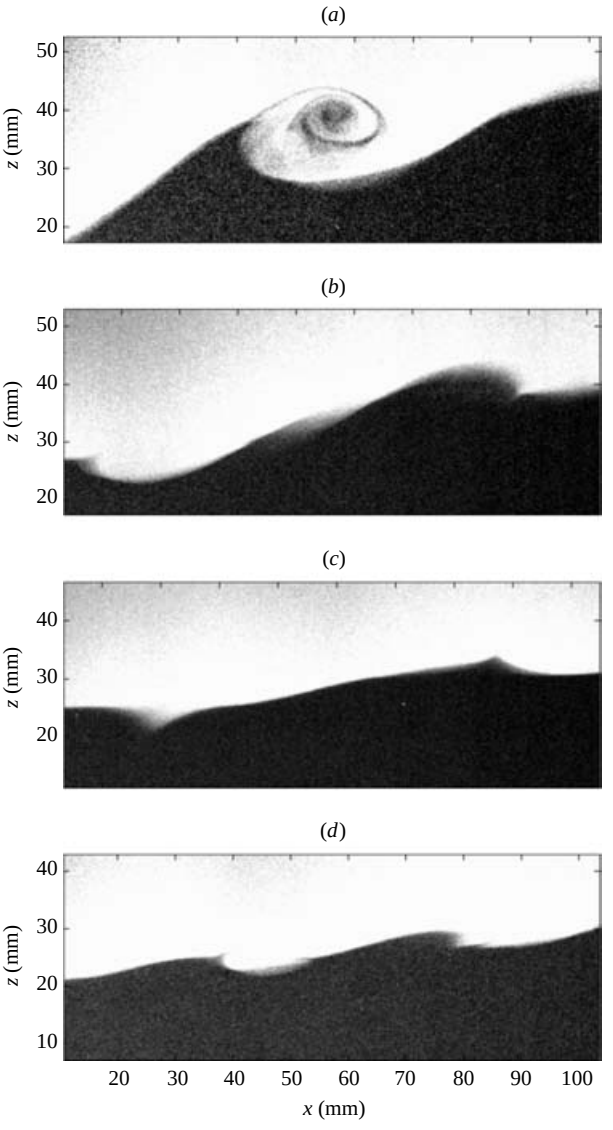

FIGURE 6. Still photographs from different parameter regimes. (*a*) Experiment S1, $J \approx 0.058$, $Re \approx 55$; (*b*) experiment S2, $J \approx 0.084$, $Re \approx 48$; (*c*) experiment S3, $J \approx 0.12$, $Re \approx 48$; (*d*) experiment S4, $J \approx 0.10$, $Re \approx 55$.

the caption, and are discussed more fully in § 4. In experiment S1 a KH instability is observed, as shown in figure 6(*a*). Large billows are formed which do not travel with respect to the mean fluid flow: the instabilities are dragged away from the centre of the contraction by the mean shear. The billows grow to large amplitude and then collapse, after which the shear flow advects fluid away from the mixed region and acts to reduce the interface thickness. Sharpening of the interface ensues, thereby decreasing stability until another perturbation forms.

Some interface perturbations in experiment S2 (where fluid height H has been decreased) exhibit features of both KH and Holmboe's instability. For instance, figure 6(*b*) captures one such instability which overturns the central density interface,

yet is travelling with respect to the mean flow. This is consistent with flows simulated by Smyth & Peltier (1991) which are close to the KH–Holmboe transition point.

By decreasing the fluid height again (experiment S3, figure 6*c*) we reach a state which clearly shows the characteristics of Holmboe's instability. The two component Holmboe modes are shown: the downward cusping wave is travelling to the left and the upward cusping mode is travelling right. The two modes are confined in their region of influence (as shown in the numerical simulations of Smyth *et al.* 1988). The large amplitude of the modes demonstrates that the disturbances are nonlinear and it will be shown below that they interact with each other during their evolution.

Experiment S4 shown in figure 6(*d*) has the same value of H as experiment S3, but double the density difference so that, according to two-layer hydraulic solution, the fluid velocities are the same as in experiment S1. The observed flow shows the character of Holmboe's instability with two oppositely propagating modes, demonstrating that the velocity difference across the interface is not the primary parameter which governs the mode of instability.

The evolution of instabilities with time is best visualized with space–time diagrams. To construct these diagrams we use a number of sequential images from experiment series A, which show the density field as indicated by the fluorescein dye. At any point in time (t) and space (x), we can define a density profile. A tanh function fitted to the density profile is used to determine the vertical position of the interface. By finding the interface position at all points in x and t we are able to plot the perturbation of the interface height from the running mean. This is done in figure 7 for experiments A1–A4.

The transition from KH to Holmboe's instability is clearly illustrated by figure 7. A signature of KH instability is that disturbances propagate away from the centre of the contraction, with the mean fluid velocity. The instabilities do not travel with constant velocity, as shown in figure 7(*a*). In contrast, the velocity of the Holmboe modes is very well defined. Theoretically these modes should have constant velocity relative to the mean shear, and to some extent this is shown in figure 7(*c*, *d*), with waves travelling slowly as they propagate towards the centre of the contraction, and speeding up as they exit the contraction. In figure 7(*b*), the x–t diagram for experiment A2, both KH and Holmboe's instability are present, particularly for early time.

3.2. *Velocity structure of instabilities*

Using PIV we obtained two-dimensional measurements of fluid velocity in the contracting channel. Figure 8(*a*) shows velocity vectors for experiment P2 which is in the KH regime. Despite some patchiness in the coverage of the vectors, one can clearly resolve several elliptical-shaped KH eddies at different stages of their evolution.

The structure of the instabilities alter at the KH–Holmboe transition. Figure 8(*b*) shows velocity vectors and the density interface position for the case close to the transition (experiment P3) with the left-travelling component mode shown. The two differences between this mode and the KH instability in figure 8(*a*) is that the streamlines in the high-vorticity region are not closed, and the mode now propagates with respect to the mean shear. Features of Holmboe modes are more clearly shown in figure 8(*c*) (experiment P5). Here two component Holmboe modes are propagating to the right. As is the case with density visualization of the waves, the region of

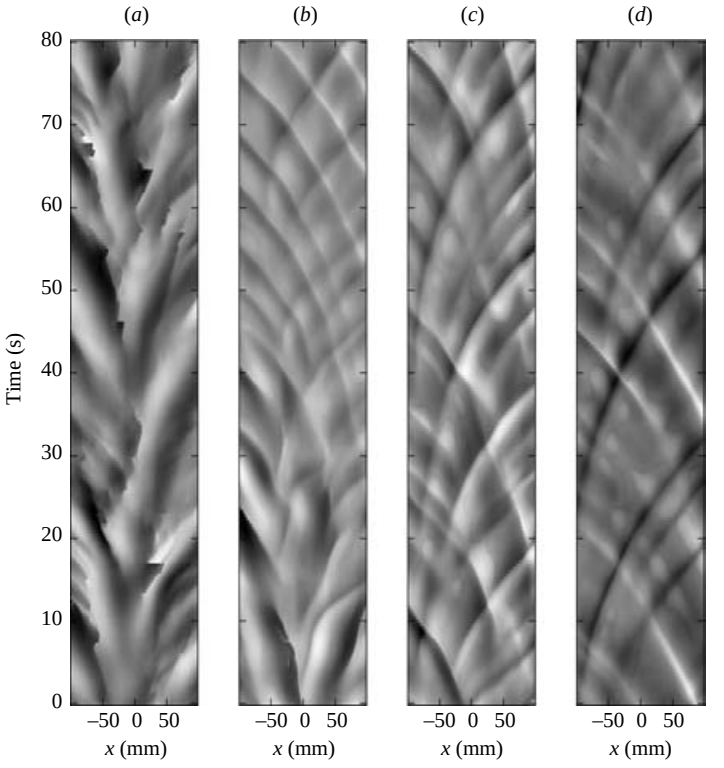

FIGURE 7. The evolution of instabilities shown in x–t diagrams. (a) Experiment A1, $J \approx 0.065$, $Re \approx 55$; (b) experiment A2, $J \approx 0.079$, $Re \approx 50$; (c) experiment A3, $J \approx 0.096$, $Re \approx 50$; (d) experiment A4, $J \approx 0.119$, $Re \approx 48$;

influence of the wave is very small. Within the confined region of perturbation, the vertical velocity is high.

The general structure of the component Holmboe modes is similar to that predicted by numerical simulations of nonlinear Holmboe instabilities (Smyth *et al.* 1988). The structural features which include a region of high vorticity on the face of the modes are observed. The modes travel slower than the fluid in the adjacent layer, so that fluid is continually passing over the top of the cusp, and the region of high vorticity sits on the lee side of the wave relative to the fast flowing fluid.

3.3. *Interactions between two component Holmboe modes*

The interaction between component modes of Holmboe's instability is of interest for several reasons. First, Smyth & Peltier (1989) demonstrate that it is during the interaction of two modes that the instability is amplified, and some mixing occurs. Secondly, if non-linear phase locking alters the point of KH–Holmboe transition, then it is possible that the component modes may be attenuated as they pass one another. It was noted by Zhu & Lawrence (2001) that whilst linear theory predicts that the waves should speed up as they approach one another, observations of Holmboe modes indicated that the converse in fact occurs. Figure 7 shows that it is difficult to see any sign of interaction between the component modes. This indicates that if phase locking of component modes is the mechanism responsible for

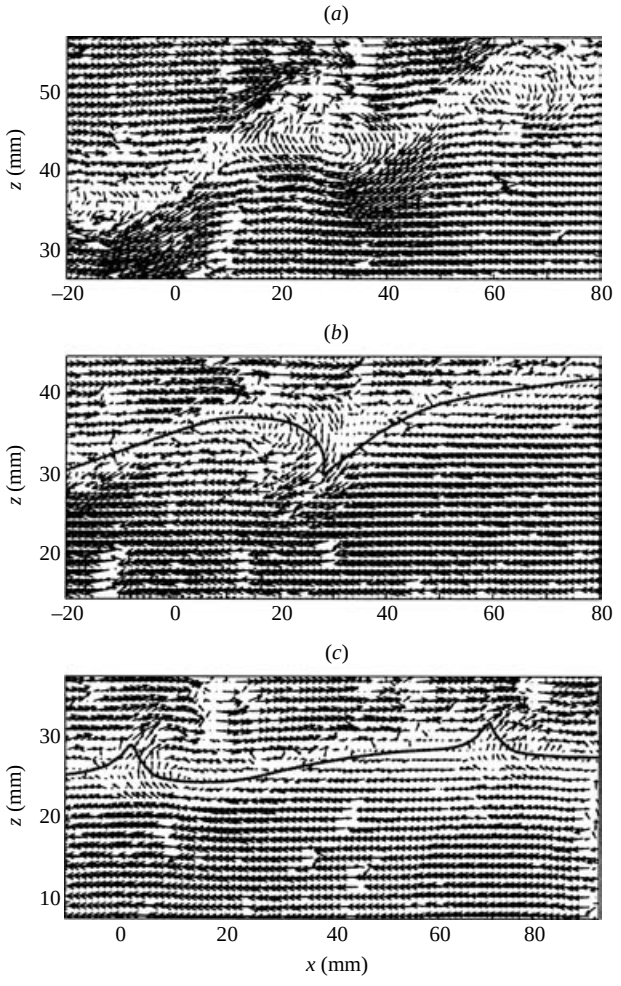

FIGURE 8. Velocity vectors for (*a*) experiment P2, $J \approx 0.073$, $Re \approx 48$; (*b*) experiment P3, $J \approx 0.083$, $Re \approx 48$; (*c*) experiment P5, $J \approx 0.118$, $Re \approx 48$. The approximate position of the density interface is shown by the solid line in (*b*) and (*c*).

KH instability, then this mechanism is not due to the gradual increased interaction of component modes. Instead, our observations support the prediction of Baines & Mitsudera (1994) that the transition to KH instability occurs when vorticity modes can communicate due to reduced J, and that the likelihood of communication is not enhanced by non-linear interaction between the component Holmboe modes.

While the mixing done by Holmboe's instability is weak, Smyth & Peltier (1991) indicate that accelerated mixing occurs in the form of a wisp of fluid being ejected through the cusp of a component mode as two modes pass one another. This wisp is observed in the present experiments, as shown in figure 6(*b*). As expected, the frequency of observations of wisping is greater near the KH–Holmboe transition. However, the occurrence of the wisp is not correlated with the interaction between component modes. This may be an indication that, as postulated by Smyth & Peltier (1991), the wisping depends upon three-dimensional effects, while the

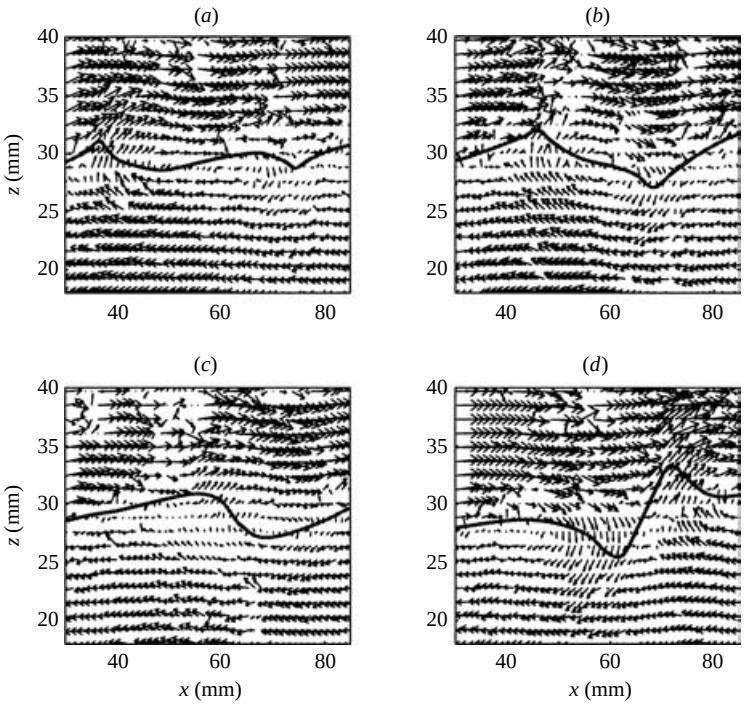

FIGURE 9. Velocity vectors for experiment P5, $J \approx 0.118$, $Re \approx 48$ showing the interaction between two component modes. The approximate position of the density interface is shown by the solid line. Each frame is separated by 1 s.

measurement techniques used here are only capable of visualizing a two-dimensional field.

The amplification of component modes just after they pass one another as described by Smyth *et al.* (1988) was tested in these experiments. In general, interacting waves amplify each other, although there is some variability in this process. The amplification of interacting modes is easiest to observe in the velocity field. An example is shown in figure 9, with four panels separated by 1 s. Panel (*a*) shows a strong right-propagating mode, with a weak left-propagating mode, both having vorticity of the same sign, just before interaction. One second later, the modes are positioned so that the two vortices produce a large single vortex. The vortex acts to kinematically amplify both component modes, as described by Baines & Mitsudera (1994). However, the modes pass one another, so that they do not form a single billow. Instead, the next frame shows that the waves continue with negligible attenuation. In this frame they appear to be linearly superposed, leaving a residual upwards vertical velocity (since the left-going disturbance is smaller), but a smaller vortex than before interaction. In panel (*d*) the two modes break free from one another. The vertical velocity field demonstrates that the right-travelling mode has increased in amplitude by 20%, and that the left-travelling mode has increased by 50%. This sort of interaction occurs frequently in the experiments, and can also be identified in the *x*–*t* plots in figure 7. The most prominent example can be seen in figure 7(*c*) at time 68 s, where a right-going mode acts to strongly amplify a left-going mode. While there is significant variability in this process, as a general rule the two modes are both amplified during the interaction. In some cases, interacting waves destroy one of the modes, although

it is once again possible that this is caused by three-dimensional effects or secondary instability.

4. Predicting modes of instability

4.1. *Scaling of stability parameters*

In this section we consider some simple scaling arguments which allow us to include the first-order effects of molecular viscosity and diffusion in determining the finite thicknesses η and δ in a hydraulic exchange flow. This, combined with knowledge of ΔU and $\Delta\rho$, can be used to predict the bulk Richardson number, the Reynolds number and the ratio of thicknesses R.

The finite thickness of the velocity interface, δ, is due to the viscous diffusion of momentum over some timescale τ, or

$$\delta \sim (\nu\tau)^{1/2}. \tag{4.1}$$

The most appropriate timescale will be related to the fluid velocity and a horizontal lengthscale L over which the two fluid layers are in contact, that is

$$\tau \sim \frac{L}{\Delta U}. \tag{4.2}$$

This can be combined with (1.1) and (4.1) to give

$$\delta \sim \frac{(\nu L)^{1/2}}{(g'H)^{1/4}}, \tag{4.3}$$

which describes the dependence of the velocity interface thickness upon external parameters.

The density interface thickness can be estimated using the same technique, replacing ν with the molecular diffusion of salt κ,

$$\eta \sim (\kappa\tau)^{1/2}. \tag{4.4}$$

The application of this argument is complicated by the density interface being thinner than the velocity interface. Therefore, the fluid velocity at the edge of the density interface will be reduced in proportion to the ratio R of the two thicknesses. For this reason, the timescale used for estimating the density interface is

$$\tau \sim \frac{L}{\Delta U(\eta/\Delta)}, \tag{4.5}$$

giving

$$\eta \sim \frac{\kappa^{1/3}\nu^{1/6}L^{1/2}}{(g'H)^{1/4}}. \tag{4.6}$$

The interface thickness is dependent on the choice of horizontal lengthscale L. The dominant horizontal lengthscale in the problem is the length of the channel so that the lengthscale is the same for both velocity and density interfaces, giving the value of the ratio of thicknesses to be

$$R \sim \left(\frac{\nu}{\kappa}\right)^{1/3} = Sc^{1/3}. \tag{4.7}$$

This estimate matches the scaling of Bejan (1995) for the growth of boundary layers in a large Prandtl number fluid, but differs from that of Smyth *et al.* (1988), because

the periodic boundary conditions in that paper mean that the differential velocity plays no role in determining the thicknesses. Instead, Smyth *et al.* (1988) estimate that $R = Pr^{1/2}$ provided that R starts at that value. Note also that Smyth *et al.* (1988) considered heat as the stratifying species, and therefore used the Prandtl number as the ratio of diffusivities, whereas in a salt-stratified fluid the Schmidt number is the relevant parameter.

We are now able to estimate the bulk Richardson number in this flow. From (1.1) and (1.3) we write

$$J = \frac{\delta}{H}, \tag{4.8}$$

and using (4.3) we obtain

$$J \sim \frac{(\nu L)^{1/2}}{g'^{1/4} H^{5/4}}. \tag{4.9}$$

The Reynolds number can be estimated from (1.1), (1.6) and (4.3):

$$Re \sim \frac{(g'H)^{1/4} L^{1/2}}{4\nu^{1/2}}. \tag{4.10}$$

The scaling arguments shown here demonstrate the dependence of stability parameters upon relevant external controllable parameters for the exchange flows considered here. By varying g' and H, both Re and J change, but R is constant. Note that δ and Re depend weakly upon both external parameters, while J varies strongly with H. Therefore we expect variations of H to be the primary cause of variations in stability. At large values of H, J will decrease, and KH billows are likely; as H is decreased we may pass through the transition to Holmboe's instability.

We now evaluate the consistency of the scaling results by directly measuring η and δ in the experiments, and determine R, J and Re using (4.7), (4.8) and (4.10) respectively. This allows comparison of linear stability theory with the observed behaviour.

4.2. *Comparison of experiments with scaling arguments*

An image of the velocity profile measured by falling potassium permanganate crystals for experiment K2 is shown in figure 10. This image shows the symmetrical form of the interface with the exception of the influence of the bottom boundary layer. The interface thickness measured by (2.2) gives $\delta = 6.2 \pm 0.3$ mm, and the solid line in figure 10 shows the maximum slope of the interface. The experimental uncertainty here is generated from uncertainty in estimating the maximum gradient for use in the denominator in (2.2). By measuring δ from several profiles in each of experiments K2–K4, we are able to plot δ against the right-hand side of (4.3) in figure 11. In this case, the solid line shows (4.3) using a scaling coefficient of 1.55. Therefore, we represent the interface thickness by

$$\delta \approx 1.5 \frac{(\nu L)^{1/2}}{(g'H)^{1/4}}. \tag{4.11}$$

Measurements of density interface thickness defined according to (2.1) were taken from experiments S2–S4 by fitting a tanh function to vertical profiles of light intensity. The results from these three measurements including experimental uncertainties are plotted in figure 12 against the predicted thickness of the gradient region in the fluorescein concentration profile from (4.6). Note that we have taken the molecular diffusion of fluorescein to be $\kappa_F = 2000$ (Ware *et al.* 1983) in the calculation. The large experimental error is due to the effect of refraction of light in the interfacial region,

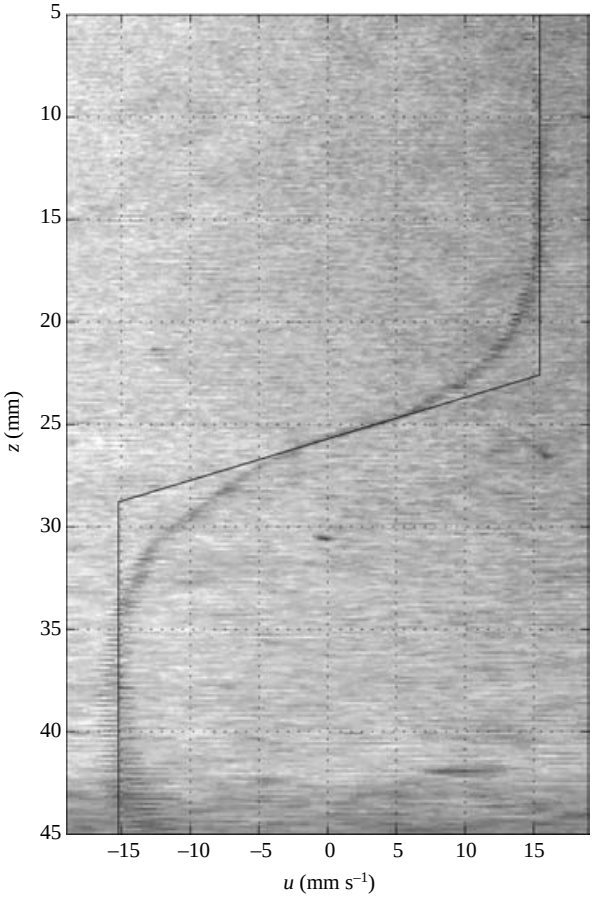

FIGURE 10. Snapshot of the velocity profile experiment K2, before the onset of instability. The solid line shows the idealized interface giving $\delta \approx 6.2$ mm.

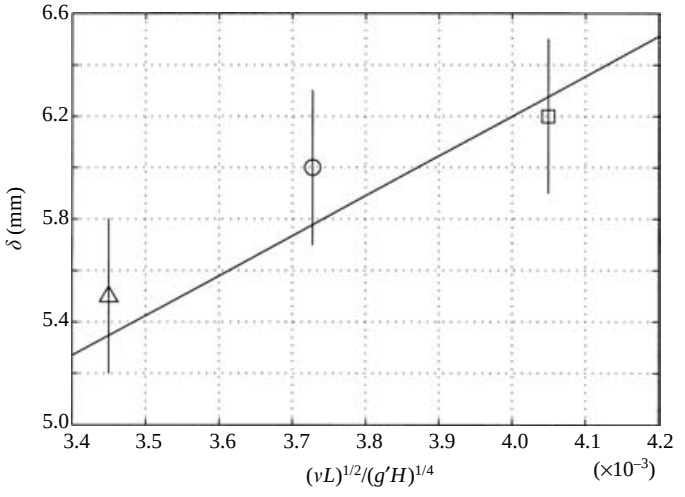

FIGURE 11. Measurements of δ for experiments K2 (□), K3 (○), K4 (△). The solid line is the relationship given by (4.11).

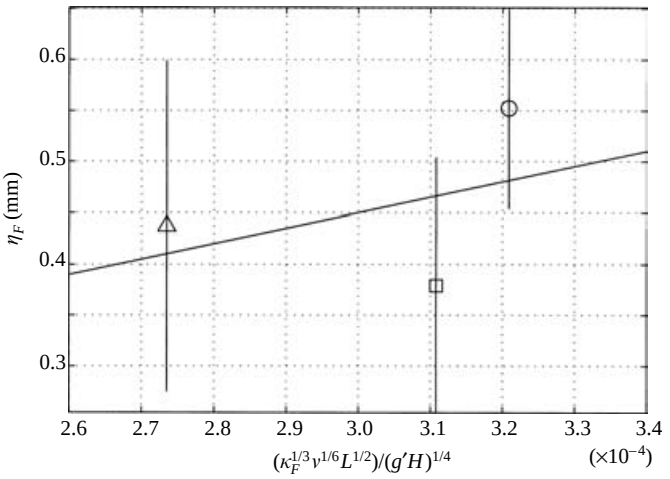

FIGURE 12. Measurements of η for experiments S2 (□), S3 (○), S4 (△). The solid line is the relationship given by (4.12).

and makes it difficult to validate the weak dependence of η_F upon the parameters g' and H; however the evidence shown here is consistent with a scaling coefficient of 1.5 in (4.6). From this we infer the density interface thickness η (in mm) to be

$$\eta \approx 1.5 \frac{\kappa^{1/3}\nu^{1/6}L^{1/2}}{(g'H)^{1/4}}. \tag{4.12}$$

The ratio of thicknesses can be calculated from (4.11) and (4.12) to give

$$R \approx Sc^{1/3} \approx 8. \tag{4.13}$$

The results in (4.11) and (4.12) are not consistent with measurements of δ and η in experiments K1 and S1 respectively, when fluid height is $H = 90\,\text{mm}$. In these cases, interface thicknesses before the onset of instability are $\delta \approx 13 \pm 1\,\text{mm}$, and $\eta \approx 2.2 \pm 0.4\,\text{mm}$, which are both a factor of 4 greater than expected. The onset of instability occurs early in this experiment, as soon as the steady exchange begins. We hypothesize that because of the decreased stability of this experiment, the flow is required to pass through a number of unstable states as the interface sharpens. Therefore it becomes unstable before reaching the quasi-steady background state predicted by (4.11) and (4.12).

By combining (4.11) with (4.8) we can write an expression for the bulk Richardson number J in the exchange flow,

$$J \approx 1.5 \frac{(\nu L)^{1/2}}{(g'H^5)^{1/4}}. \tag{4.14}$$

We use (4.10) to predict the variation of Reynolds number in the flow. Again we substitute (4.11) to give

$$Re \approx 0.4 \frac{L^{1/2}(g'H)^{1/4}}{\nu^{1/2}}. \tag{4.15}$$

Note that there is quite a weak dependence of Reynolds number on experimental parameters, so that the range of Reynolds numbers is quite small. Nonetheless, the Reynolds numbers in the flow are of order 50 so that we can expect a significant

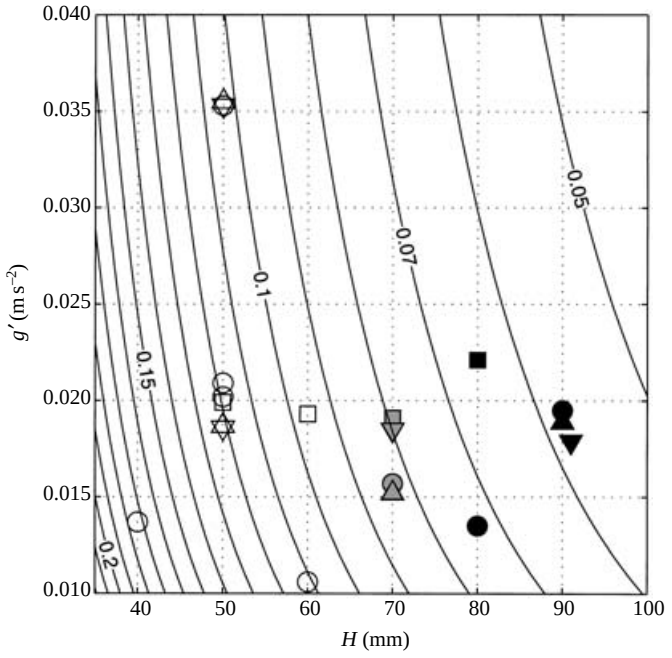

FIGURE 13. The value of g' versus H for each experiment. Contours show levels of constant J. Experiments A (□), P (○), S (△) and K (▽). The open symbols indicate Holmboe's instability was observed, and black symbols indicate KH instability. For experiments in which both forms of instability were observed the symbol is grey.

reduction in amplification rates compared to the inviscid prediction (as seen in figure 4, and in Browand & Wang 1972; Smyth *et al.* 1988).

4.3. *Comparison between observed instabilities and linear theory*

A summary of the observed instabilities is shown in figure 13, where the functional dependence of J on g' and H is shown by contours of constant J, and the type of instability observed for each experiment is indicated. The open symbols denote the formation of Holmboe's instability, and there is a clear trend for this to occur at high values of J. At lower values of J, the black symbols denote KH instability. In some experiments both types of instability were observed and this is shown by grey symbols. These data show a well-defined transition from KH–Holmboe's instability to occur at $J \approx 0.08$. There is a significant difference between the observed transition point and that predicted by linear stability. The solution of (1.7) with $R = 8$ and $Re = 50$ yields a transition point at $J \approx 0.05$. This disparity between the observed and predicted transition points cannot be explained by experimental uncertainties.

Linear stability also gives predictions about the wavelengths and phase speeds of Holmboe modes. Phase speeds are defined relative to the mean flow, and thus we measure the absolute phase speeds from $x-t$ diagrams such as figure 7, and use the difference between the absolute speed of left- and right-going instabilities to infer the relative phase speeds. Measurements of wavelength in the experiments are both difficult and subjective for two reasons. First, the absolute phase speeds are a function of position so that absolute wavelengths vary in space. Therefore we measure the frequency of instabilities at the centre of the contraction for comparison with

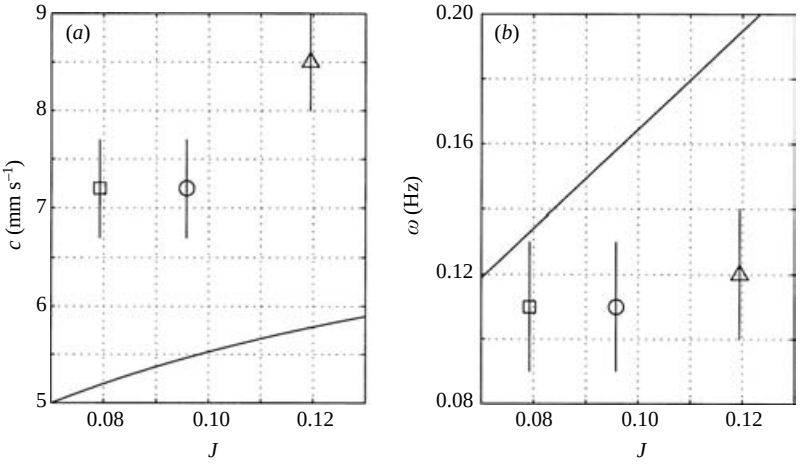

FIGURE 14. Comparison of predicted and observed (*a*) phase speed and (*b*) frequency of Holmboe modes for experiments A2 (□), A3 (○), A4 (△). Predictions are obtained by solving (1.7) with $R = 8$ and $Re = 50$.

theory. Secondly, as instabilities grow to finite size one needs to decide a threshold amplitude which distinguishes genuine instabilities from smaller disturbances. Thus the measured frequencies have significant experimental uncertainty. Predictions are compared to observed phase speeds (*a*) and frequency (*b*) in figure 14. The data in figure 14 clearly show that the observed phase speeds are higher and frequency lower than the linear stability prediction. This result is not surprising considering that linear stability theory does not accurately predict the type of instability which occurs.

There are some elements of linear stability theory which are consistent with the experiments. The KH–Holmboe transition point is both well-defined and repeatable, and can be controlled by external parameters. But quantitative predictions such as the position of the transition point, the phase speed and frequency of instabilities are inaccurate. The implications of this are discussed further in the following section.

5. Discussion

The experiments presented in this paper demonstrate several features of Holmboe's instability and the KH–Holmboe transition which have not been investigated in the laboratory before. Measurements of the density and velocity fields in the region of instabilities show many features similar to previous numerical simulations of Holmboe's instability. One feature which differed from numerical simulations was a wisp of fluid being ejected from the cusp of Holmboe's instability, which in the simulations was correlated with the interaction of two component Holmboe modes, but in these experiments was found to occur randomly. It is likely that three-dimensional effects play a role in generating this feature, and thus its role in two-dimensional simulations is expected to be different.

Observations of the KH–Holmboe transition show a strong dependence on the height of fluid in the exchange flow. This feature is at first startling, but can be reconciled by scaling arguments which predict that the bulk Richardson number (which governs linear stability) is strongly dependent on H, the fluid height, as shown

in (4.14), and depends weakly upon reduced gravity. In contrast, the Reynolds number and interface thicknesses vary only weakly with either height or reduced gravity.

Using the above-mentioned scaling, combined with direct measurements, it is possible to determine values of bulk Richardson number J, Reynolds number Re and the ratio R of velocity to density interface thickness in the experiments. One is then able to predict the phase speed and frequency of Holmboe's instability, as well as the value of J at which the transition from KH to Holmboe's instability will occur. However, here we find a significant discrepancy between the predictions and observations of all three of the above quantities, which cannot be reconciled by experimental uncertainty. This result compares unfavourably with many previous experiments on shear instability (such as Browand & Wang 1972; Scotti & Corcos 1972; Thorpe 1973; Koop & Browand 1979; Lawrence *et al.* 1991). In all these experiments good agreement was found between linear theory and the properties of the most unstable mode. However, these experiments were performed using techniques where an unstable configuration was produced by design, and instabilities were observed growing upon this initial state. In the current experiments the instabilities are part of an evolving flow: they grow into non-linear disturbances and thus mix the stable stratification and alter the velocity profile, while forces act to push the flow back towards an unstable state. The result is that there is no stable initial state. Instabilities are growing upon a field which has some memory of previous instabilities and is therefore both spatially and temporally variable. We present no simple theory which can account for all of these factors, but note that linear stability theory does capture some essential elements of the system. It is worth noting that Zhu & Lawrence (2001) performed similar experiments in which agreement between observed and predicted instabilities are adequate; however these experiments are performed at higher Richardson number ($J = [0.3, 1.0]$) where non-linearity and mixing play a smaller role.

These results demonstrate that caution is required when applying linear theory to determine the stability of observed flows. In a flow where perturbations grow, they reach a finite size and thereby alter the background state. It is the altered state which is generally observed in experiments. Thus it may not be possible to estimate the stability of a flow based on observed flow variables.

It has been proposed (Caulfield 1994; Baines & Mitsudera 1994) that the two component modes which make up Holmboe's instability are each produced by the interaction of two modes, one travelling on the density interface, and one on the vorticity interface. According to this theory, KH instability forms when the two vorticity modes (one from each component Holmboe mode) lock phase. While Smyth & Peltier (1991) observe the phase locking of two non-linear component Holmboe modes which are fired towards one another, the present experiments show no evidence that component modes attenuate each other. Phase locking of two vorticity modes should not be confused with phase locking of component Holmboe modes. When J is sufficiently small that phase locking of vorticity modes can occur, the growth of KH instability outstrips the growth of Holmboe's instability, so that in an evolving flow such as that described here, Holmboe's instability is not observed.

We are grateful for the role played by Kraig Winters in assisting us to set up this experiment, as well as suggestions from Michael Barry in conducting the experiments and writing up these results. The original draft of this manuscript was significantly improved due to suggestions from three referees to whom we are

grateful. The first author was supported by an Australian Postgraduate Award and Jean Rogerson Postgraduate Supplementary Scholarship for the duration of this work. The experimental program was supported by the Australian Research Council.

REFERENCES

Armi, L. 1986 The hydraulics of two flowing layers with different densities. *J. Fluid Mech.* **163**, 27–58.

Armi, L. & Farmer, D. M. 1987 A generalization of the concept of maximal exchange in a strait. *J. Geophys. Res.* **92**, 14679–14680.

Baines, P. G. & Mitsudera, H. 1994 On the mechanism of shear flow instabilities. *J. Fluid Mech.* **276**, 327–342.

Bejan, A. 1995 *Convection Heat Transfer*. John Wiley and Sons.

Browand, F. K. & Wang, Y. H. 1972 An experiment on the growth of small disturbances at the interface between two streams of different densities and velocities. In *Intl Symp. on Stratified Flows*, pp. 491–498. Novosibirsk, USSR: ASCE.

Caulfield, C.-C. P. 1994 Multiple linear instability of layered stratified shear flow. *J. Fluid Mech.* **258**, 255–285.

Collins, D. A. & Maslowe, S. A. 1988 Vortex pairing and resonant wave interactions in a stratified shear layer. *J. Fluid Mech.* **191**, 465–480.

Cowen, E. A. & Monismith, S. G. 1997 A hybrid digital particle tracking velocimetry technique. *Expts. Fluids* **22**, 199–211.

Dalziel, S. B. 1991 Two layer hydraulics: a functional approach. *J. Fluid Mech.* **223**, 135–163.

Gregg, M. C. & Özsoy, E. 2002 Flow, water mass changes, and hydraulics in the Bosphorus. *J. Geophys. Res.* **107** (C3), 10.1029/2000JC000485.

Haigh, S. P. & Lawrence, G. A. 1999 Symmetric and nonsymmetric Holmboe instabilities in an inviscid flow. *Phys. Fluids* **11**, 1459–1468.

Hazel, P. 1972 Numerical studies of the stability of inviscid stratified shear flows. *J. Fluid Mech.* **51**, 39–61.

Helfrich, K. L. 1995 Time-dependent two-layer hydraulic exchange flow. *J. Phys. Oceanogr.* **25**, 359–373.

Hogg, A. M., Ivey, G. N. & Winters, K. B. 2001*a* Hydraulics and mixing in controlled exchange flows. *J. Geophys. Res.* **106** (C1), 959–972.

Hogg, A. M., Winters, K. B. & Ivey, G. N. 2001*b* Linear internal waves and the control of stratified exchange flows. *J. Fluid Mech.* **447**, 357–375.

Holmboe, J. 1962 On the behaviour of symmetric waves in stratified shear layers. *Geofys. Publ.* **24** (2), 67–113.

Howard, L. N. 1961 Note on a paper of John W. Miles. *J. Fluid Mech.* **10**, 509–512.

Klaassen, G. P. & Peltier, W. R. 1985 The onset of turbulence in finite-amplitude Kelvin–Helmholtz billows. *J. Fluid Mech.* **155**, 1–35.

Koop, C. G. & Browand, F. K. 1979 Instability and turbulence in a stratified fluid with shear. *J. Fluid Mech.* **93**, 135–139.

Koppel, D. 1964 On the stability of a thermally stratified fluid under the action of gravity. *J. Meth. Phys.* **5**, 963–982.

Lawrence, G. A. 1990 On the hydraulics of Boussinesq and non-Boussinesq two-layer flows. *J. Fluid Mech.* **215**, 457–480.

Lawrence, G. A. 1993 The hydraulics of steady two-layer flow over a fixed obstacle. *J. Fluid Mech.* **254**, 605–633.

Lawrence, G. A., Browand, F. K. & Redekopp, L. G. 1991 The stability of a sheared density interface. *Phys. Fluids* A **3**, 2360–2370.

Miles, J. W. 1961 On the stability of heterogeneous shear flows. *J. Fluid Mech.* **10**, 496–508.

Pawlak, G. & Armi, L. 1998 Mixing and entrainment in developing stratified currents. *J. Fluid Mech.* **424**, 45–73.

Scotti, R. S. & Corcos, G. M. 1972 An experiment on the stability of small disturbances in a stratified free shear layer. *J. Fluid Mech.* **52**, 499–528.

Smyth, W. D., Klaassen, G. P. & Peltier, W. R. 1988 Finite amplitude Holmboe waves. *Geophys. Astrophys. Fluid Dyn.* **43**, 181–222.

Smyth, W. D. & Peltier, W. R. 1989 The transition between Kelvin–Helmholtz and Holmboe instability: An investigation of the overreflection hypothesis. *J. Atmos. Sci.* **46**, 3698–3720.

Smyth, W. D. & Peltier, W. R. 1991 Instability and transition in finite-amplitude Kelvin–Helmholtz and Holmboe waves. *J. Fluid Mech.* **228**, 387–415.

Smyth, W. D. & Winters, K. B. 2002 Turbulence and mixing in Holmboe waves. *J. Phys. Oceanogr.* (in press).

Stevens, C. L. & Coates, M. J. 1994 Application of a maximised cross correlation technique for resolving velocity fields in laboratory experiments. *J. Hydraul. Res.* **32**, 195–212.

Thorpe, S. A. 1973 Experiments on instability and turbulence in a stratified shear flow. *J. Fluid Mech.* **61**, 731–751.

Ware, B. R., Cyr, D., Gorti, S. & Lanni, F. 1983 Electrophoretic and frictional properties in complex media measured using laser light scattering and fluorescence photobleaching recovery. In *Measurement of Suspended Particles by Quasi-elastic Light Scattering* (ed. B. E. Dahneke), pp. 255–289. Wiley.

Winters, K. B. & Riley, J. J. 1992 Instability of internal waves near a critical level. *Dyn. Atmos. Oceans* **16**, 249–278.

Winters, K. B. & Seim, H. E. 2000 The role of dissipation and mixing in exchange flow through a contracting channel. *J. Fluid Mech.* **407**, 265–290.

Wood, I. R. 1970 A lock exchange flow. *J. Fluid Mech.* **42**, 671–687.

Zhu, D. Z. & Lawrence, G. A. 2000 Hydraulics of exchange flows. *J. Hydr. Engng* **126** (12), 921–928.

Zhu, D. Z. & Lawrence, G. A. 2001 Holmboe's instability in exchange flows. *J. Fluid Mech.* **429**, 391–409.